

pubs.acs.org/JACS Article

Self-Assembly Mechanism of Complex Corrugated Particles

Lanqin Tang, Thi Vo, Xiaoxing Fan, Drew Vecchio, Tao Ma, Jun Lu, Harrison Hou, Sharon C. Glotzer,* and Nicholas A. Kotov*



Cite This: J. Am. Chem. Soc. 2021, 143, 19655–19667



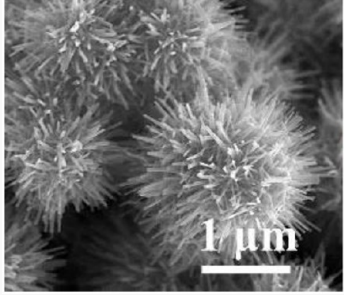
ACCESS

Metrics & More



SI Supporting Information

ABSTRACT: A variety of inorganic nanoscale materials produce microscale particles with highly corrugated geometries, but the mechanism of their formation remains unknown. Here we found that uniformly sized CdS-based hedgehog particles (HPs) self-assemble from polydisperse nanoparticles (NPs) with diameters of 1.0–4.0 nm. The typical diameters of HPs and spikes are 1770 \pm 180 and 28 \pm 3 nm, respectively. Depending on the temperature, solvent, and reaction times, the NPs self-assemble into nanorods, nanorod aggregates, low-corrugation particles, and other HP-related particles with complexity indexes ranging from 0 to 23.7. We show that "hedgehog", other geometries, and topologies of





highly corrugated particles originate from the thermodynamic preference of polydisperse NPs to attach to the growing nanoscale cluster when electrostatic repulsion competes with van der Waals attraction. Theoretical models and simulations of the self-assembly accounting for the competition of attractive and repulsive interactions in electrolytes accurately describe particle morphology, growth stages, and the spectrum of observed products. When kinetic parameters are included in the models, the formation of corrugated particles with surfaces decorated by nanosheets, known as flower-like particles, were theoretically predicted and experimentally observed. The generality of the proposed mechanism was demonstrated for the formation of mixed HPs via a combination of CdS and Co_3O_4 NPs. With unusually high dispersion stability of HPs in unfavorable solvents including liquid CO_2 , mechanistic insights into HP formation are essential for their structural adaptation for applications from energy storage, catalysis, water treatment, and others.

■ INTRODUCTION

Micrometer-scale highly corrugated particles with nanoscale structural features have attracted widespread academic attention because their unusual geometry associated with special physical and chemical properties is an asset for heterogeneous catalysis, ¹⁻⁷ sensing, ⁸ drug delivery, ⁹⁻¹¹ environmental remediation, ¹²⁻¹⁴ and optics. ¹⁵ The high surface area combined with the simplicity of particle recovery makes particles with "spiky" surfaces compelling for many applications. The corrugated surface also leads to singularity points at the apexes, which results in unusual scattering and nonlinear optical effects for even the modest corrugations. ¹⁶⁻²¹ The morphology of particles with spikes is often likened to geometrically analogous living structures exemplified by sea urchins, flowers, pollen grains, dendritic cells, and numerous viruses. In fact, spiky spheres are a common theme in biology and appear to be a universally exploited geometry for controlling particle—particle interactions. ¹⁵

For simplicity, we will refer to highly corrugated nanostructured colloids as hedgehog particles (HPs), implying that they will be covered with characteristic stiff, rod-like nanoscale spikes around a submicrometer core that reduce attractive van der Waals (vdW) forces between them.¹⁵ If the surface corrugations are shaped as nanosheets, they will be termed flower-like particles (FLPs). Both HPs and FLPs can be synthesized for a variety of inorganic nanomaterials indicating the generality of the physicochemical processes underlying their formation. While some of the spiky morphologies for SiO₂-coated CdTe nanowires were observed as far back as in 2004,²² the mechanisms of their self-assembly remain largely unknown. Such commonality presents a fundamental question about the relationship between complexity and thermodynamic favorability. The physicochemical reasons why these colloids spontaneously produce more complex structures despite much simpler options, such as disorganized clumps or smooth supraparticles (SPs),^{23,24} are worthy of investigation for fundamental curiosity and advanced particle technologies.

Received: May 27, 2021 Published: November 16, 2021





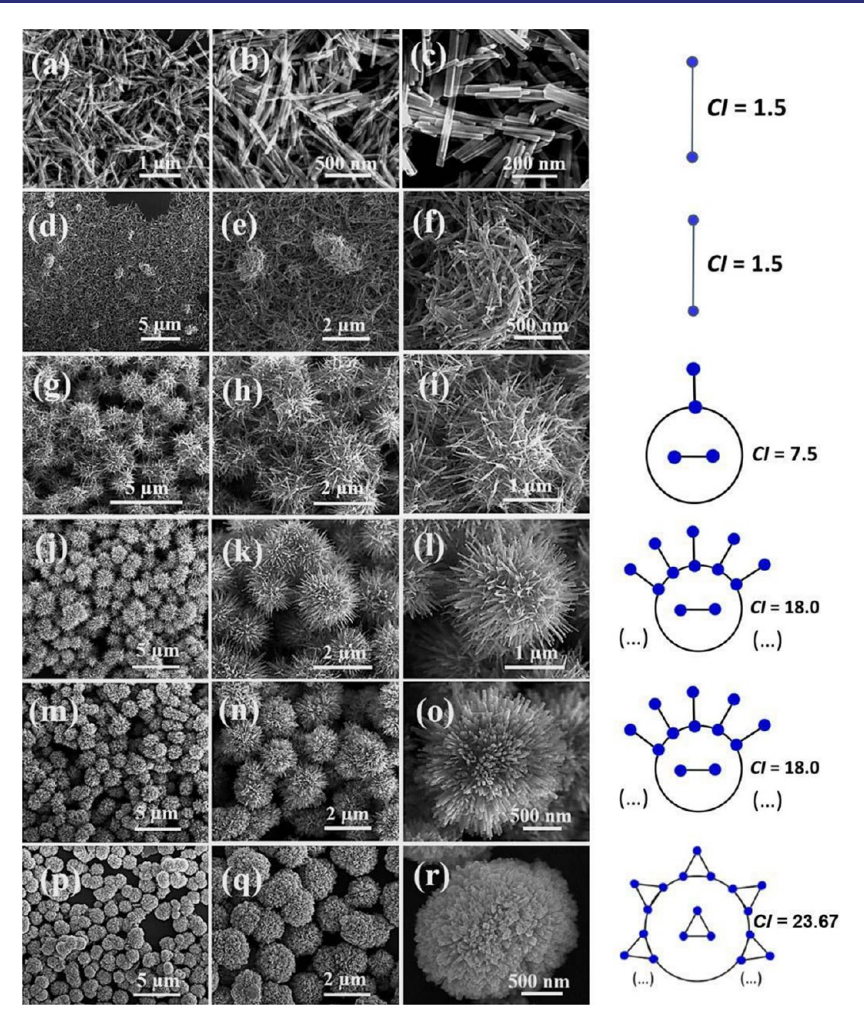


Figure 1. SEM images of complex nanostructured microparticles from CdS assembled at different V_R at 160 °C for 20 h with corresponding GT representations: (a-c) $V_R = 0.0$ NRs; (d-f) $V_R = 0.33$ agglomerated NRs; (g-i) $V_R = 0.66$ HPs with random orientation of the spikes; (j-l) $V_R = 1.0$ fully formed HPs; (m-o) $V_R = 1.5$ fully formed HPs; (p-r) $V_R = 3.0$ low corrugation FLPs. Notes for GT representations. Free and randomly agglomerated NRs are represented by a K_2 graph (i.e., node-edge-node) as in (a-f). The K_2 graph inside a loop in (g-o) represents randomly positioned NRs assembled into a spherical SP of nonrandom size. Single K_2 graph connected by one node to a loop as in (g-i) represents NRs connected by one end to a microscale core of SPs in random orientation. A quasi-infinite sequence of K_2 graphs connected to a loop in (j-o) represents the nonrandom orientation of the NRs with all the spikes being in radial orientation with respect to the particle surface. K_3 graph (i.e., three nodes connected into a triangle) inside a loop in (p-r) represents nanosheets assembled into a spherical SP of nonrandom size. A quasi-infinite sequence of K_3 graphs connected to a loop represents nanosheets connected to the loop in nonrandom radial orientation with respect to the surface of the SP.

■ RESULTS AND DISCUSSION

Experimental Phase Diagrams of Complex Corrugated Particles. A variety of cadmium sulfide (CdS) nanostructures have been synthesized, including some uniquely structured particles.²⁵⁻³⁰ We use the formation of CdS HPrelated structures as a model system to gain in-depth understanding of the mechanisms and nanoscale processes leading to them. Cadmium diethyldithiocarbamate served as a single-source precursor for these particles' decomposition in ethylenediamine (EA) and water (see the Methods section) solutions. We found that the morphology of produced CdS micro- and nanoparticles (NPs) can vary dramatically from dispersed individual NPs and nanorods (NRs) to lowcorrugation FLPs and HPs with long and sharp nanoscale bristles (Figure 1). Among the experimental parameters tested in this study (Table S1 and Figure S1), the morphology of CdS nanostructures was strongly dependent on the water-to-EA volume ratio (V_R) . When no water is present, $V_R = 0$, NRs with a length of 200–500 nm are formed after 20 h of thermolysis at 160 °C (Figure 1a–c). The NRs start to assemble as more water is added. For instance, agglomerates of NRs can be seen at $V_{\rm R}=0.33$ (Figure 1d–f). A transition from NRs to their spheroidal aggregates is observed at $V_{\rm R}=0.66$ (Figure 1g–i). Unlike HPs, the orientation of the needles is not yet perfectly radial, and many of them clump together, imparting some randomness in their organization. When $V_{\rm R}$ is increased to 1.0 and 1.5, distinct HPs with an average diameter of 1770 \pm 180 nm are produced. At these higher $V_{\rm R}$ ratios, all needles acquire nearly perfect radial orientation compared to particles with $V_{\rm R}=0.66$. The three-dimensional reconstructions of fully formed HPs obtained by TEM tomography (Video S1) confirm the geometry observed in SEM.

Further increased water content to $V_{\rm R}=3.0$ results in the formation of microparticles with an average diameter of 1800 \pm 200 nm that display shorter spikes and smaller corrugation. The surface features noticeably change shape, transitioning from rod-like to sheet-like structures (Figure 1r and Figure

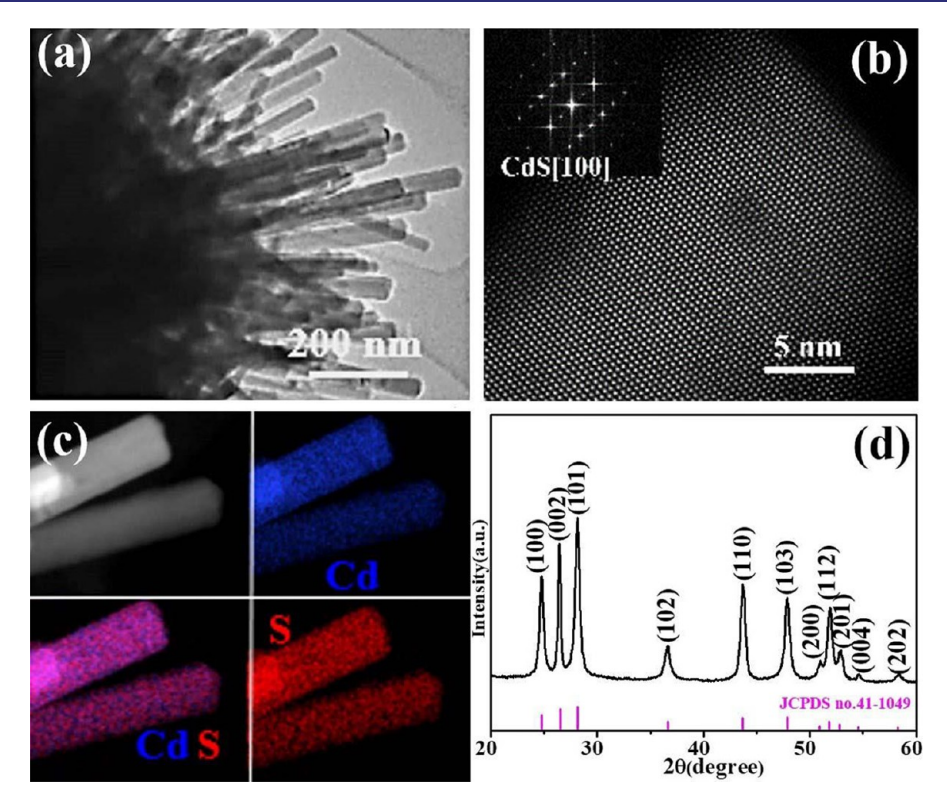


Figure 2. Atomic structure of CdS HPs: (a) TEM image, (b) HR-STEM image of spike, (c) STEM-EDS maps, and (d) XRD pattern.

S2). This morphology makes them similar to that of a wide range of FLPs; an increase of temperature to $t=180\,^{\circ}\text{C}$ accentuates the transition of the spikes to sheet-like morphology (Figures S1 and S2).

Increased V_R also results in increased complexity of the products. Graph theory (GT) applied to nanoscale materials³¹ allows one to (a) represent particle structure by using the same toolbox as that used to describe molecular structures in chemistry and (b) enumerate their complexity by using a previously defined complexity index (CI) and other GT enumerators.³¹ CI values are surprisingly high in this study to many possible alternatives that can be observed for particles of similar sizes. The CIs of HPs and FLPs are 18.0 and 23.6667 \approx 23.7, respectively, while those of random agglomerates are 0, NRs are 1.5, porous nanoshells are 4.0, and smooth uniformly sized porous SPs^{11,30} are between 2.0 and 6.0. Note that the GT representation of the spiky particles obtained at $V_R = 0.33$ is different than those for particles obtained at $V_{\rm R}$ = 0.66 and $V_{\rm R}$ = 1.5 because the structure of the former is described as spiky spheres with semirandomly oriented spikes connected by one end to the particle core. The fully formed HPs feature spikes with uniform radial orientation are represented by the GT model with a quasi-infinite sequence of multiple spikes. The transition from random to nonrandom orientation of spikes leads to a concomitant increase in complexity. Also note that despite increased CI, FLPs obtained at $V_R = 3.0$ show decreased corrugation, which indicates that these two structural characteristics are not linearly related.

We also note that the particles with $V_{\rm R} \ge 0.66$ are uniform in size, which is not the case for NRs or their agglomerates at $V_{\rm R}$ = 0.33; this may be associated with a self-limiting pathway for the formation of SPs whose assembly from polydisperse charged NPs is restricted by electrostatic repulsion. ²³ Self-limiting self-assembly pathways restricted by electrostatic

repulsion are observed for numerous particle assemblies, in both $2D^{32-35}$ and $3D.^{23,36-38}$ CdS HPs obtained after 20 h at 160 °C with $V_{\rm R}$ of 1.0 and 1.5 were investigated further because they are representative of both highly corrugated and complex particles. Insights into the nanoscale structure of HPs were obtained from TEM images, STEM-EDX images, and XRD patterns (Figure 2). An HR-STEM image of spikes shown in Figure 2b revealed the growth direction of the nanospikes is along the [001] axis of the hexagonal crystal. The selected area electron diffraction (SAED) pattern from the spike reaffirmed its crystalline nature and showed that the spikes are single crystals with a=4.149 Å and c=6.731 Å (JCPDS Card No. 41-1049) and with Cd and S uniformly distributed throughout the spikes (Figure 2c,d).

The typical length of spikes in HPs is ~300 nm. Note that the central part of corrugated particles is too dense for electron beams to penetrate, creating some uncertainty about the length of the spikes. We performed ion beam milling of the particle to obtain the cross-sectional image. As one can see from Figure S12a, the inner part of the HPs is essentially a SP made from NRs, with the GT representation of their core structure given in Figure S12c. Thus, there is some part of the NRs that is embedded in this SP core, but concerning the properties, GT representation, and assembly model, this embedded part is less relevant than the part of the spike-forming NRs that extends beyond the core surface forming the radial "halo" of nanoscale corrugations.

Maintaining $V_{\rm R}=1.0$, the HPs syntheses were performed at several temperatures. The diameters of spikes were found to be 31 ± 4 , 28 ± 3 , 18 ± 2 , and 12 ± 1 nm for 180, 160, 140, and $120\,^{\circ}{\rm C}$, respectively (Figure 3; see the Methods section), indicating the possibility of varying particle morphology by changing the reaction temperature. A similar trend between spike diameter and the temperature was also observed for $V_{\rm R}=$

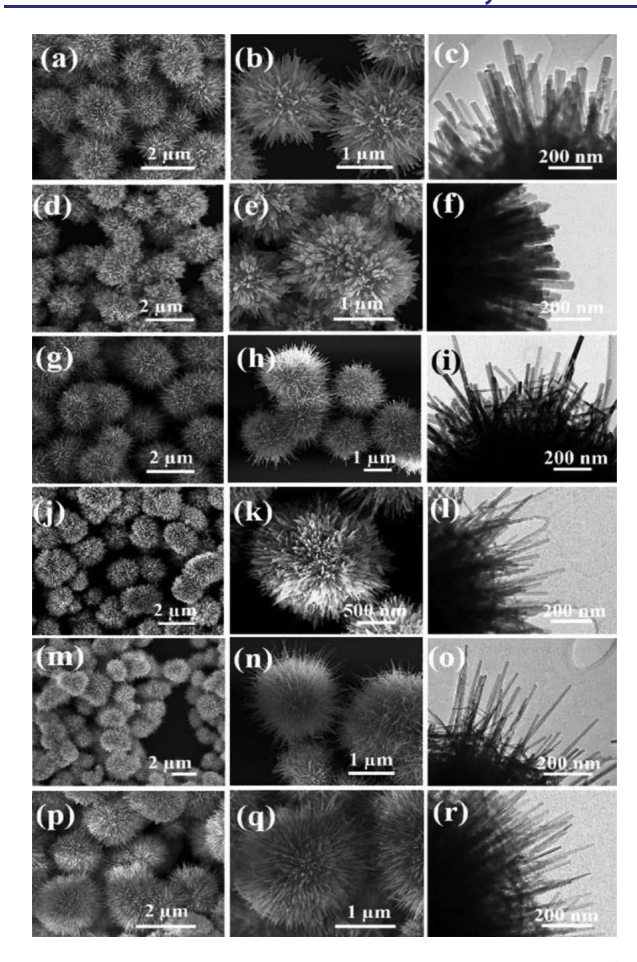


Figure 3. SEM and TEM images of CdS HPs obtained at 180 °C (a–f), 140 °C (g–l), and 120 °C (m–r) for 20 h with V_R = 1.0 (a, b, c, g, h, i, m, n, o) and 1.5 (d, e, f, j, k, l, p, q, r).

1.5 (Figures 3 and 4a). Note that the spikes formed at lower temperatures display distinct tapered shapes (Figure 30,r). The

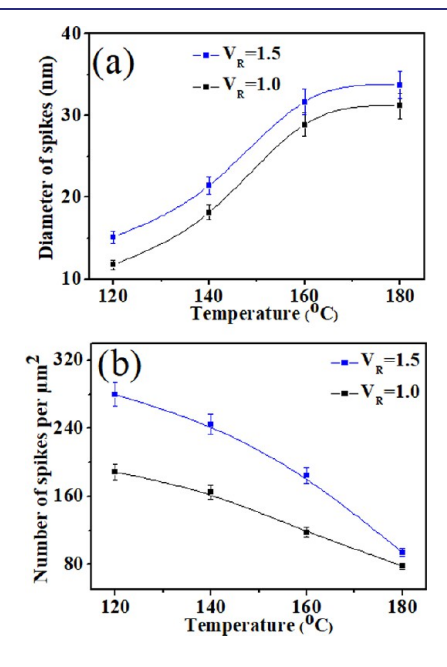


Figure 4. (a) Diameter and (b) areal density of CdS spikes, η_A , for HPs synthesized at different temperatures with $V_R = 1.0$ and $V_R = 1.5$.

areal density of spikes, $\eta_{\rm A}$ (in number per $\mu{\rm m}^2$), markedly increases with decreased temperature. For example, the $\eta_{\rm A}$ of HPs obtained at 160 °C is nearly 2 times larger than that of HPs synthesized at 180 °C (see the Methods section). The $\eta_{\rm A}$ also increases with the addition of water. Keeping the temperature constant at 120 °C, the change of $V_{\rm R}=1.0$ to $V_{\rm R}=1.5$ results in $\eta_{\rm A}$ increasing from 190 \pm 9 to 280 \pm 14 $\mu{\rm m}^{-2}$ (Figure 4b). The complexity index for all HPs remains the same, CI = 18.0, because the GT representation of the particles does not depend on the spike diameter, length, or surface density as long as the spike remains a single monocrystalline rod and maintains the nonrandom organizational pattern.

Dispersion in Organic Solvents and Liquid CO_2 . The variation of V_R and reaction temperature allows one to tune the degree of corrugation and complexity, which are essential for many of the desired physical, chemical, and biological properties. For example, mitigation of attractive forces counteracting long-range electrostatic repulsion engenders the unusually high dispersion stability of HPs in both aqueous and nonpolar solvents. Similar to previous observations of ZnO-based HPs in high ionic strength media, dispersions of CdS-based HPs remain stable in the presence of 0.5–2.0 M NaCl (Figure 5a,b), despite the high mass that causes them to

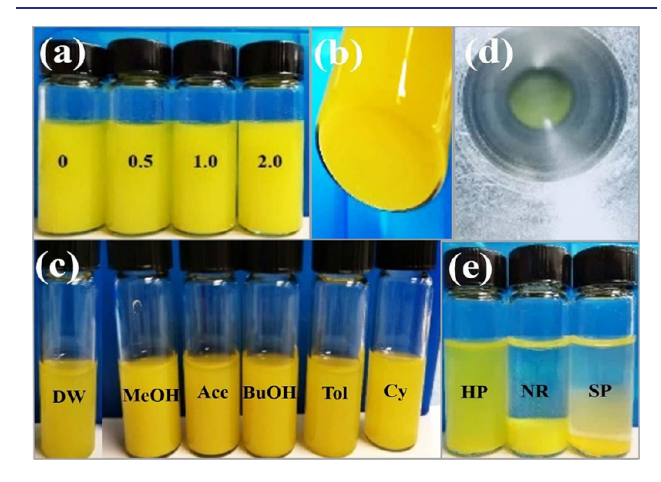


Figure 5. Photographs of aqueous dispersions of CdS HPs in (a, b) 0.0, 0.5, 1.0, and 2.0 M NaCl solution; (c) water and organic solvents: DW, distilled water; MeOH, methanol; Ace, acetone; BuOH, butanol; Tol, toluene; Cy, cyclohexane; (d) liquid CO_2 and (e) HPs, NRs, and SPs in distilled water after sedimentation for 3 h.

sediment slowly under gravity. Unlike particles with smooth surfaces under similar conditions, the sediments can be easily redispersed by shaking because the HPs do not clump together, remaining separated by the spikes. This colloidal property is essential for a variety of chemical reactions and technological processes.

The ability of CdS HPs to disperse in liquid media was studied by using five different organic solvents. In addition to water, CdS HPs can be dispersed in methanol, acetone, butanol, toluene, and cyclohexane (Figure 5c). Even in toluene, dispersions of CdS HPs are stable for dozens of minutes and easily return to the suspended state by shaking. Among unfriendly solvents, CdS HPs disperse best in butanol with no sediment after at least 2 h. CdS HPs can also be dispersed in liquid $\rm CO_2$ (Figure 5d). To some degree, it is no longer surprising that hydrophilic CdS HPs disperse in liquid $\rm CO_2$ that is hydrophobic because these HPs disperse in similar

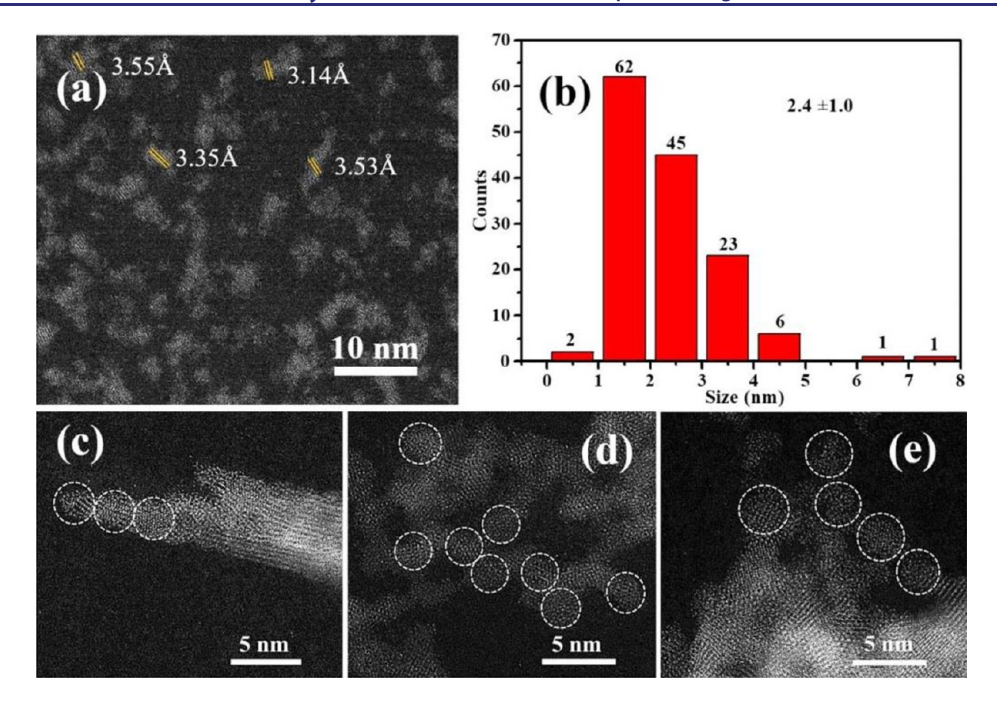


Figure 6. Initial NPs obtained after 1 day of incubation at t = 25 °C: (a) STEM images and (b) size distribution of the NPs in the dispersion. (c, d, e) STEM images of the precipitate were obtained after centrifugation.

fashion in toluene. The stability of the dispersion in liquid CO_2 and toluene is, however, not as high as in butanol.

The effect of particle topology and complexity on the colloidal stability can be vividly seen when comparing dispersions of different forms of CdS on the phase diagram in Figure 1. After being dispersed in water for about 3 h, CdS NRs and smooth noncorrugated SPs settle to the bottom while many HPs remain suspended (Figure 5e).

Mechanism of HP Self-Assembly. The early stages of the reaction, when no microscale products or precipitates are formed (Figure S4 and Table S2), inform about the system pathways leading to the formation of complex highly corrugated particles. Multiple conditions were imaged by electron microscopy to identify the precursors to HPs, NRs, and other nanostructures in this reaction.

When the reaction is slowed by carrying it out at 25 °C (room temperature), we found that NPs are the dominant product after 1 day of incubation (Figure 6a). The dispersion displays an average particle size of 2.4 nm and has a wide size distribution with a standard deviation of 1.0 nm (Figure 6b). These NPs are nevertheless crystalline; the crystal lattice spacings observed in STEM images are 3.55, 3.53, 3.35, and 3.14 Å, which can be assigned to the (100), (100), (002), and (101) planes of hexagonal CdS (PDF #41-1049). Centrifugation of these dispersions results in isolation of a small amount of precipitated matter where the early NP assemblies aligned into NRs can be found (Figure 6c–e).

It is well-known that NPs can self-assemble into nanostructures with continuous crystallinity via oriented attachment, ⁴⁰ a nonclassical crystallization pathway. ⁴¹ Specifically, CdTe ⁴⁰ PbS, ⁴² and ZnO NPs ⁴³ with diameters, dispersity, and crystallinity similar to those of CdS NPs in Figure 6 were shown to spontaneously assemble into single-crystalline NRs and nanowires. The intermediates in those self-assembly processes were NP chains and short rods that are similar to the intermediates observed for CdS HPs in Figures 6 and 7 as well as Figures S5–S9. On the basis of the current and

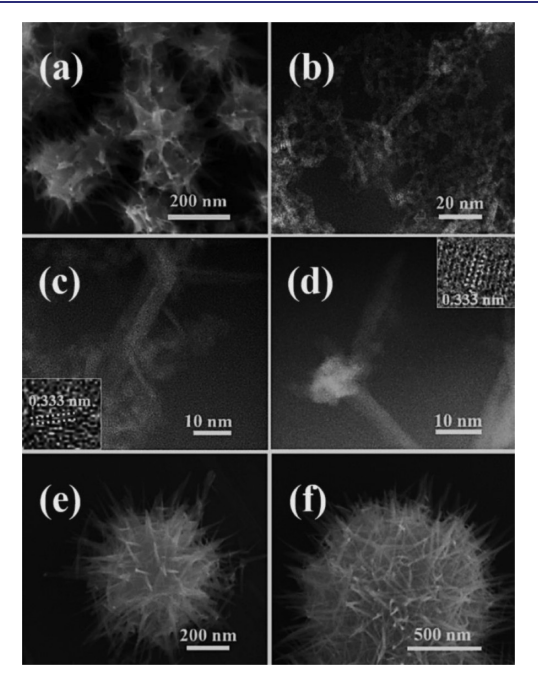


Figure 7. SEM and STEM images of CdS nanostructures obtained at 160 $^{\circ}$ C with $V_{\rm R}=1.0$ and reaction times of 45 min (a–d), 55 min (e), and 75 min (f).

past data, one can confidently conclude that NRs, HPs, and other particles shown in Figures 1 and 3 as well as Figure S1 are the products of NP self-assembly into chains followed by oriented attachment. Higher temperature accelerates the process and allows the system to access different assembly states but does not change the nature of the building blocks as can be seen by the presence of NPs at all stages of the assembly except the reaction mixtures when HPs are fully formed (Table S2). The similarity of the mechanism of the self-assembly process at different temperatures can be justified by the following observations: (a) NP building blocks are the same at

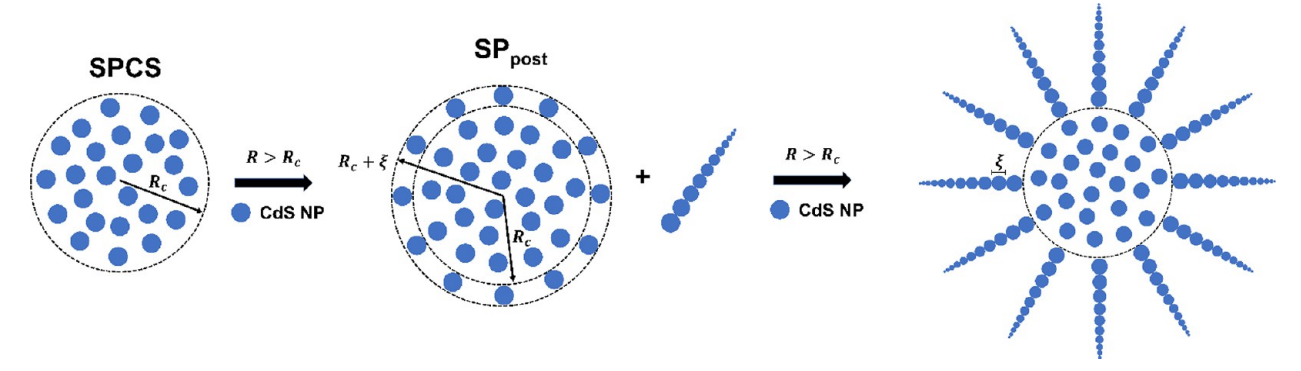


Figure 8. Pictorial representation of the self-assembly process leading to SPCS and the spike formation. NPs aggregate up to size R_c representing SPCS. Beyond R_c electrostatic repulsion selects for building blocks of increasingly smaller sizes to add to the growing SPCS, giving rise to the spikes. The NPs forming SPCS self-assemble into NRs in the process oriented attachment. This transition occurring simultaneously with self-assembly is not represented in this diagram for simplicity.

low and high reaction temperatures (Figure 6d vs Figure S5a); (b) crystalline NRs forming from NPs are the same at low and high reaction temperatures (Figure 6c vs Figure S7); (c) intermediate self-assembled structures representing SP cores (Figure S6 vs Figure 7a and Figure S5b) are the same at low and high reaction temperatures. The NPs, NRs, and intermediates were examined at 25 and 160 °C.

We also followed the progress of the NP assembly into HPs at different reaction times allowing the samples to cool naturally from $160\,^{\circ}\text{C}$ to room temperature. Small quasi-HPs form (Figure S8a) after a reaction time of 25 min. They highlight the tendency of NRs to align in the direction perpendicular to that of the growing SP cores but remaining in fairly irregular orientation for each other, which is confirmed by different microscopy techniques including TEM tomography (Video S1). Besides illustrating the process of the HP formation, these data also support the choice of GT models in Figure 1 and particularly the GT representation of the HP core as the K_2 graph inside the loop indicating the random orientation of NR in the HP cores.

Increasing the reaction time to 45 min, CdS HPs with an average size of 300 ± 50 nm are predominantly observed as well as small numbers of NRs and clusters of entangled NR (Figure 7a–d and Figure S9). The interplanar spacing of $d=0.333 \pm 0.001$ nm corresponds to that of the (100) plane in wurtzite CdS, which remained unchanged throughout the reaction time (insets in Figure 7c,d). With increased reaction time from 45 to 55 min, the NR clusters grow to become more isotropic (Figure 7e). A distinct phase transition from largely disorganized NR clusters to HPs occurs between 55 and 75 min of reaction time (Figure 7f). Extending the reaction time beyond 80 min has no influence on the morphology of the assembled nanostructures or the shape of the CdS spikes (Figure S8b–d), which is consistent with the attainment of a (local) thermodynamic equilibrium state for the system.

Theory and Simulations of NP Assembly into Complex Particles. The multiplicity of nanostructures resulting from varying temperature and reaction time shows that the self-assembly of NPs into NRs is followed by the secondary assembly of the latter into entangled NR clusters. The uniformity of the resulting HPs is consistent with the thermodynamic constraints arising as the growth of HPs via oriented attachment of NPs described in the preceding section produces larger HPs. Considering prior studies of self-organization of NPs into SPs, 31,44 the overall mechanism of

formation can be described as a case of self-limiting self-assembly when physical dimensions of the assembled structures are limited by the electrostatic repulsion. To extend this idea and explain the transition from the simple SPs with CI = $2-6^{31}$ to complex particles represented by HPs and FLPs with CI = 18 and 23.7, respectively, we explore further the dependence of electrostatic repulsion on SP size.

Let us consider the thermodynamics of NP-NP interactions dictating their assembly into larger particles. 45,46 The NPs are attracted to each other due to van der Waals interactions with a characteristic distance of 0.5-1.5 nm⁴⁷ that includes nonlocal nonadditive effects distinguishing NPs from microparticles.⁴⁸ With each additional NP or NR attaching to the central core, an extra δ^{\pm} charge is added onto the growing superstructure, resulting in the gradual increase of repulsive interactions with a characteristic distance of 1-10 nm depending on Debye screening length and ionic strength of the media. 49,50 The attractive forces (which may include other short-range interactions such as hydrogen and coordination bonds) compete with electrostatic repulsion and, in the absence of oriented attachment processes, result in the alignment of NPs into chains, ^{50,51} sheets, ⁵² or SPs. ²³ As with many electrostatically restricted self-assembly systems, ^{23,32–38} the net charge of the assembly eventually outcompetes the attractive interactions when it reaches a critical size, R_c . An assembly of NPs that reaches R_c will be termed a supraparticle of critical size (SPCS). Once R_c is reached, subsequent NPs that are added to the SPCS are selected from the polydisperse pool of NPs available in the media. To help with clarity, we will refer to the growing SP with size $R < R_c$ and $R > R_c$ as SP_{pre} and SP_{post} respectively. For NP attempting to attach to SPpost, the attractive interaction between the SP_{post} and the NP must be sufficient to overcome the local repulsion for the NP additions to occur (Figure 8). This process may select the NPs depending on its size, shape, and total charge. Electron microscopy images in Figure 6a and Figure S5a show no preferential shape of the NPs, so for simplicity we will consider them to be spherical within the framework of this study. In terms of NP size and total charge, larger NPs exhibit higher net charges. Therefore, relative to larger particles, smaller NPs with less overall charge are favored for attachment due to weaker electrostatic repulsions between the NP and SP_{post}. For a single spike, this process iteratively selects smaller and smaller NPs to add to SP_{post} resulting in tapered spikes formation. In locations with multiple concurrently growing spikes, the high electrostatic repulsions between neighboring spikes prevent NP addition to the side of each spike. This limits NP addition to only the tips of growing spikes, where the local electrostatic repulsion is weakest. In other words, electrostatics tunes SP_{post} growth such that distinct, tapered spikes are formed via successive additions of decreasingly smaller NPs (Figure 9).

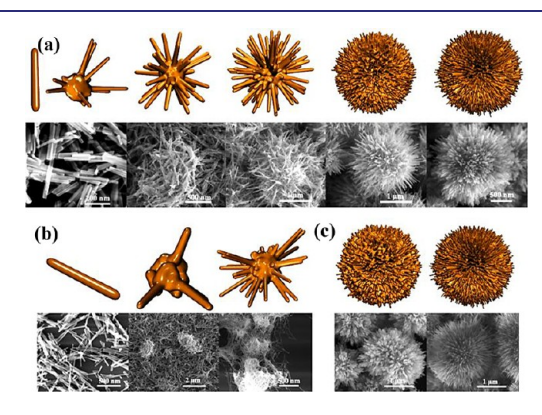


Figure 9. Comparison of simulated and experimental particles morphologies. (a) Morphology change as a function of increasing $V_{\rm R}$ from left to right at 160 °C. (b) Morphology change as a function of decreasing temperature—180, 160, and 100 °C (left to right)—for constant $V_{\rm R}=0.33$. (c) Morphology change as a function of decreasing temperature going from left (180 °C) to right (120 °C) for constant $V_{\rm R}=1.5$.

The potential energy, U(r), of sequential addition of NPs to SP_{post} when electrostatic repulsion competes with van der Waals attraction to select NPs from a polydisperse pool can be given as

$$U(r) \sim \xi^{3}(r)\phi(r) + \frac{n_{\mathrm{T}}(r)}{r/\sigma} e^{-\kappa r}$$
(1)

where r is the radial distance from the surface of SPCS with the size of R_c , ξ is the correlation size (that is, the size of the NPs being added, at a distance r), $\phi(r)$ is the local concentration of NPs at a distance r from the surface of the SPCS, κ is the inverse of the Debye screening length of the electrolyte around the NP, σ is the dimensionality conversion constant commensurate with the units of κ and R_c , and n_T is the total charge of the growing SP_{post} assembly after each successful NP addition. Equation 1 requires expressions for ξ , ϕ , and n_T (a brief derivation is provided in the Supporting Information for

the relevant mathematical details). The correlation size ξ can be defined by balancing van der Waals attraction driving NP attachment and electrostatic repulsion. Here, we take the standard scaling form for van der Waals attraction $U_{\rm vdW} \sim \frac{C}{\xi^6}$ and a Yukawa screened potential for electrostatic repulsion $U_{\rm Yukawa} \sim \frac{n_{\rm c}n_{\rm x}}{\xi/\sigma} {\rm e}^{-\kappa\xi}$, where $n_{\rm c}$ is the charge contribution from the growing SP_{post}, $n_{\rm x}$ is the charge contribution from the NP, and C is London coefficient of the particle—particle interaction potential. Noting that C is related to the Hamaker constant via the relationship $A \sim \pi^2 k_{\rm B} T C \rho_1 \rho_2$, we can substitute C for A in $U_{\rm vdW}$ and define $U_{\xi} = U_{\rm vdW} + U_{\rm Yukawa}$ to give

$$U_{\xi} \sim \frac{n_{c}n_{x}}{\xi/\sigma} e^{-\kappa\xi} + \frac{A}{T\xi^{6}}$$
(2)

where we dropped unitary constants such as π , $k_{\rm B}$, and ρ . Minimization of eq 2 with respect to ξ in the limit of $n_{\rm T} \gg n_x$ and noting that $n_{\rm T} = n_{\rm c} + n_x$ yields

$$\xi(r) \sim A^{1/5} T^{-1/5} \kappa^{1/5} n_T^{-1/5}(r)$$
 (3)

The physical picture underpinning our theoretical development is such successive attachment of NPs of decreasing sizes form tapered spikes. Geometrically, such spikes are analogous to conical frustums growing from the surface of an SPCS. Therefore, we can write the total number of NPs within the growing SP_{post} as $n_{\rm T} \sim \xi^2 r \sigma^{-3}$. S3,54 Rearranging for ξ , plugging into eq 3, and solving for $n_{\rm T}$ yields

$$n_{\rm T}(r) \sim A^{2/7} T^{-2/7} \kappa^{2/7} r^{5/7} \sigma^{-15/7}$$
 (4)

The local concentration $\phi(r)$ is simply $\phi(r) \sim n_{\rm T}(r)\sigma^3[r(R_{\rm c}+\xi)^2]^{-1}$.

We conducted Monte Carlo (MC) simulations of NP aggregation based on the standard Metropolis sampling algorithm using U(r). Snapshots of simulations show distinct analogy with the experimental SEM images as a function of increasing $V_{\rm R}$ (Figure 9) when we varied the dielectric constant of the media that determines the Debye screening length and the electrostatic potential.

To study the temperature dependence, we perform MC simulation for a range of temperature in the limit of low and high water content, yielding the morphologies shown in Figures 9b and 9c, respectively. High temperature shifts toward the electrostatics dominated the regime for NP attachment, making it increasingly more difficult for multiple spikes to grow within the same region of space and reducing the spike count

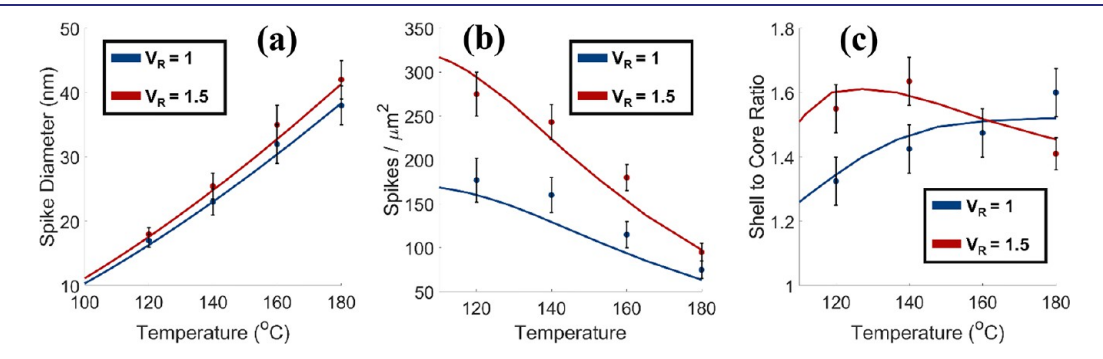


Figure 10. Comparison of simulated and experimental geometrical parameters of HPs. Scatter points are experimental measurements from Figure 4. Solids lines indicate computed values. Each line corresponds to the measured value for different V_R used in synthesis as a function of temperature, as indicated by the legend. (a) Diameter of spikes. (b) Number of spikes per μ m². (c) Ratio of the shell to core size. The more detailed description of experimental data was obtained according to the Methods section.

per unit area. As such, particle morphologies transition from high-quality HPs to NRs aggregates to single NRs. Conversely, increasing $V_{\rm R}$ reduces electrostatic repulsion relative to attraction, giving rise to the opposite morphological trend. All of the relevant trends observed in simulations match well with experimental observations for spike diameter, spike counts per unit area, and the ratio of the maximum HP diameter (defined by the longest spike) to the mean HP size computed by averaging overall spike lengths on the particle (Figure 10a—c).

Furthermore, our thermodynamic theory captures the different phases of particles forming from CdS. Here, they are classified as four broad phases—NRs, NR aggregates (NR_A), HPs, and low corrugation particles (i.e., SPs)—that are formed when van der Waals interactions dominate over electrostatic repulsion and no charge-based selection of attaining NPs takes place. Using the fraction of well-defined spikes as an enumerator of particle morphologies, we can categorize the resulting structures across the entire parameter space of κ , A, and T (Figure 11a,b). The transition between

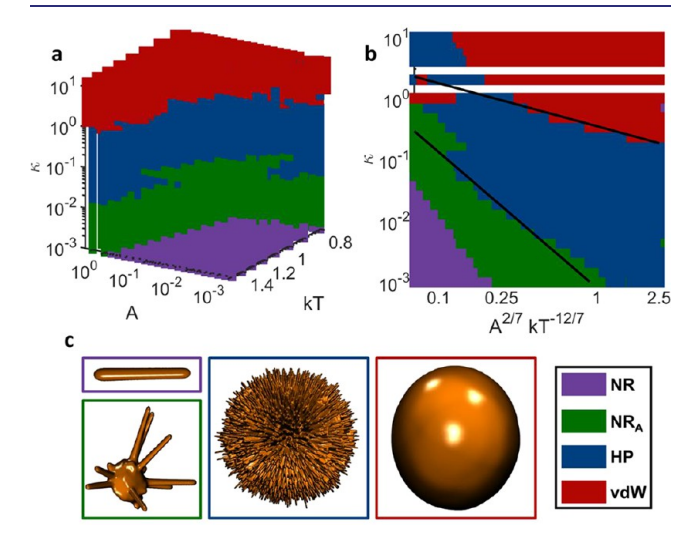


Figure 11. Phase diagrams of self-assembled particles in (a) 3D phase and (b) 2D phase format. Black line plots predicted phase boundaries. The scaling relation defined by eq 10 from the Supporting Information was used to convert a 3D phase plot to its more convenient 2D version. (c) Representative morphologies for each self-assembles phases of particles from NRs: single NR; NR agglomerate, NR_A; HP, low-corrugation supraparticle assembled from multiple NPs self-assembled into NRs, vdW.

different assembly morphologies can be understood as occurring when the combination of parameters is such that van der Waals attraction is on par with electrostatic repulsion. Specifically, the transitions from spike aggregates to "spherical" low corrugation particles occur when van der Waals attraction completely dominates. In this limit, there is no size-selective addition to the $\mathrm{SP}_{\mathrm{post}}$ growth front, thereby bypassing the formation of spikes in favor of NP aggregation (Figure 11c).

We performed an additional analysis of the temporal evolution of the self-assembled structures as the system evolves from NR aggregates to fully formed HPs (Figures S10 and S11). We observe analogous morphologies of self-assembled structures in simulations and experiments as a function of increasing growth time (Figure S10). The

theoretical predictions of the narrow size distribution of spikes compare well with the experiment (Figure S11).

Controlling Self-Assembly by Modulation of Electrostatic Interactions. We performed HP assembly in media with five different concentrations of NaCl (0.1, 0.25, 0.5, 1.0, and 2.5 M) to probe in more detail the role of electrostatic interactions in the self-assembly of complex particles and to provide additional of validation of our theory (Figure 12). Equation 1 implies that variation of the inverse screening length κ is expected to have a strong effect on the strength of electrostatic interactions. Small values of κ correspond to stronger repulsion given the same center-to-center distance between particles. This is synonymous with weak screening and thick Debye layers around NPs, nanospikes, and SPCS, which are expected to increase the electrostatic repulsion and favor larger assemblies with more complex (e.g., spiky) architecture. Increasing the salt content in the reaction media reduces the net charge on NPs, which will favor the formation of larger HPs with thicker spikes. Indeed, the predicted and observed structures of the formed nanostructured microparticles correspond very well—the diameter of the spikes is steadily increasing with ionic strength (Figure 12f). Furthermore, since varying the EA/water ratio (V_R) tunes the screening lengths in experiments, we map V_R to its theoretical counterpart κ . A slice of the phase diagram at constant A matches well with the overlaid map of the experimental data points (Figure 13).

These findings emphasize that electrostatic repulsion competes with van der Waals attraction (and other short-range attraction forces) between NPs to iteratively sculpt the formation of thinner and thinner spikes growing radially outward from the center of the microparticle. Irrespective of the source of charge or attractive interactions for NPs, the net effect remains the same—a balance between long-range electrostatic repulsion and short-range attraction.

Assembly of Corrugated Particles with Diffusion Limitations. The assembly model being considered so far describes the addition of NPs to the growing SPSC without reaction rate and/or diffusion limitations: that is, without effects of hydrodynamics. In our earlier model, once a NP of the preferred size (and thus charge) finds its way to the SP_{post} growth front, it will always be added to the growing particle. However, there can be situations where either the attachment reaction rate is too slow or diffusion is too fast, causing NPs to diffuse away from the SP_{post} growth front before it can attach to the growing particle. Such hydrodynamic effects can reduce corrugation in the resultant particle as well as change the spike shape, favoring the formation of FLPs. In other words, how fast a particle attaches to the SP_{post} modulates the formation of HPs vs FLPs. A more comprehensive model that spans both assembly regimes must necessarily consider how reaction rate alters NP assembly. Incorporating this effect into the theory yields the following modified relationship for $n_{\rm T}(r)$ (see the Supporting Information)

$$n_{\rm T}(r) \sim \frac{A^{2/7} \kappa^{2/7} r^{5/7} \sigma^{-15/7} + A l \eta^{-1} r^{1/\gamma - 5}}{1 + l \eta^{-1} r^{1/\gamma}}$$
 (5)

where η is the solvent viscosity, l is the distance between an NP in solution and the SP_{post} front, and γ is the reaction rate governing NP attachment. ⁵⁶ Here, it is important to note several features regarding eq 5 relative to eq 4. For fast reactions, $\gamma \to \infty$. The new term in the denominator reduces

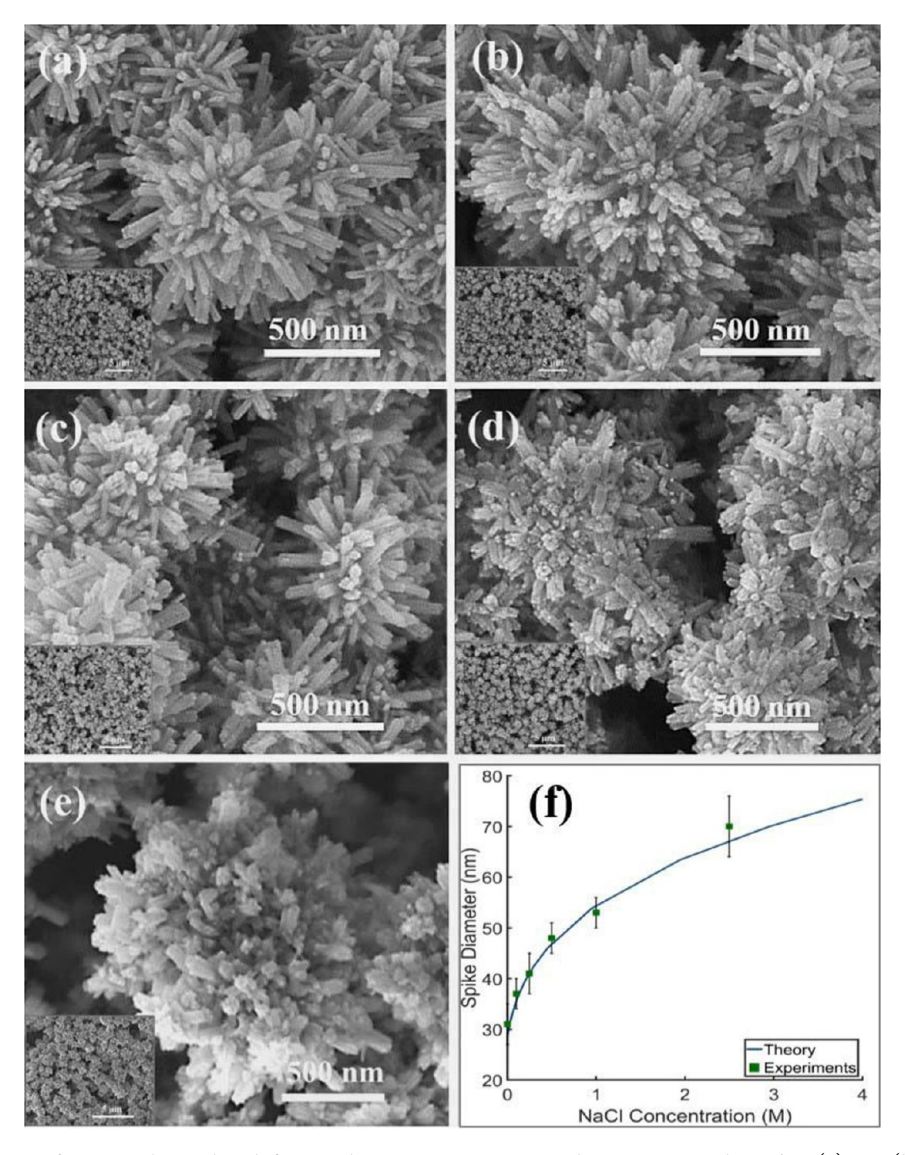


Figure 12. (a) SEM images of HPs synthesized at different salt concentration prepared at $V_R = 1.0$ and 160 °C: (a) 0.1, (b) 0.25, (c) 0.5, (d) 1.0, and (e) 2.5 M. (f) Theoretical prediction of spike diameter compared to experimental measurements.

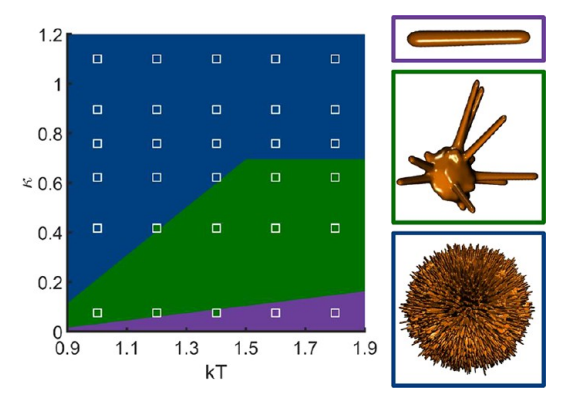


Figure 13. Projection to the $kT-\kappa$ plane at constant $A_{\rm H}$ of the phase diagram overlaid for specific particle morphologies (see also Figure 11).

to a constant. The second term in the numerator becomes of order r^{-5} . Generally, $r\gg 1$ in the regime of spike formation/growth for HPs, and thus the r^{-5} the term becomes negligible relative to the $r^{5/7}$ term. As such, eq 5 reduces to eq 4 for fast

reactions, and we recover the formation of HPs. However, for slow reactions, inclusions of the possibility for a NP failing to attach to the SP_{post} and diffusing away from the growth front result in FLPs (Figure 14). These results suggest that hydrodynamics determines the relative number of NPs that can be incorporated into the growing SP_{post} . Doing so creates situations when repulsion between spikes is weak enough to

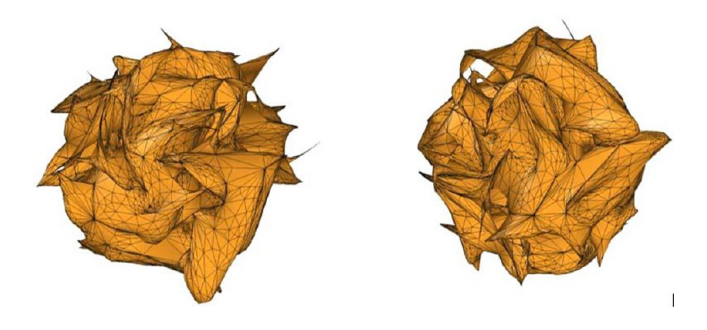


Figure 14. Simulation of FLP assembly.

enable them to merge during the growth process, giving rise to connected sheets and thus to FLPs.

Mixed Assemblies of CdS and Co₃O₄ NPs. Both growth models presented above should be applicable to NPs of any materials when screened electrostatic repulsion competes with short-range attractive interactions. One interesting possibility involves engineering complex particles from combinations of two or more different NPs. Such assembly pathway should lead to a diverse new family of complex particles and will simultaneously test the generality of the proposed mechanism.

Pursuing this hypothesis, we performed the coassembly of CdS and Co₃O₄ NPs. NPs of Co₃O₄ with a diameter of 2-5 nm stabilized by L-cysteine were synthesized separately by using a protocol published previously.⁵⁷ Co₃O₄ NPs were added to cadmium diethyldithiocarbamate precursor in an EA/ water mixture with variable weight ratios of Co_3O_4 to CdS, W_R , ranging from 0, 0.06, and 0.12 to 0.60. The synthetic conditions were those necessary for the formation of HPs, namely $V_{\rm R}$ = 1.0 and t = 160 °C for 20 h. As predicted, we observed the formation of HPs that are nearly identical with those for HPs in Figure 1j-l. The inclusion of Co₃O₄ NPs into the CdS-based HPs can be verified by EDX spectra assembled with increasing intensity of the Co band at 0.8 keV as W_R increases (Figure S13). The addition of Co₃O₄ NPs results in the gradual reduction of the diameter of spikes of the Co₃O₄ + CdS HPs from 30 ± 3 nm to 25 ± 2 , 20 ± 2 , and 16 ± 1 nm as $W_{\rm R}$ is increased from 0 to 0.06, 0.12, and 0.60, respectively (Figure 15). Increasing W_R is associated with higher surface potential in more hydrophilic amino acid covered Co₃O₄ NPs as compared to CdS NPs stabilized predominantly by organic ligands from diethyldithiocarbamate decomposition. Spike density simultaneously increased in the same progression due to the reduction of spike diameter (Figure S14).

In this new family of complex particles, we also observed the formation of FLPs for high $W_{\rm R}$ (Figure 15e) that reveal even greater complexity than HPs. In the context of this work, the formation of FLPs for ${\rm Co_3O_4}$ + CdS HPs confirms the possibility that one can obtain simultaneously high corrugation and high complexity in nanostructured microparticles, which is not obvious from the progression of the shapes in Figure 1.

CONCLUSIONS

The formation of nanostructured microparticles of high complexity originates from the thermodynamic preferences of NP attachment to the growing SPs when electrostatic repulsion competes with van der Waals attraction. When the NPs are polydisperse, such competition results in their size selection during the self-assembly and requirement for excluded volume around points on the growing SP. The size selection and NP alignment are followed by oriented attachment onto the growing assembly, resulting in monocrystalline NRs, which leads to the spontaneous formation of tapered spikes oriented perpendicularly to the microparticle surface. The experimentally observed phases of NP assemblies match nearly perfectly those predicted theoretically and observed in simulations. The generality of the proposed mechanism was demonstrated by the spontaneous formation of mixed CdS-Co₃O₄ HPs from premade Co₃O₄ NPs, making it possible to prepare particles with simultaneously high complexity and corrugation. Similar mechanisms govern the formation of FLPs with the exception that NP attachment to the points on the growing SP surface is influenced by local

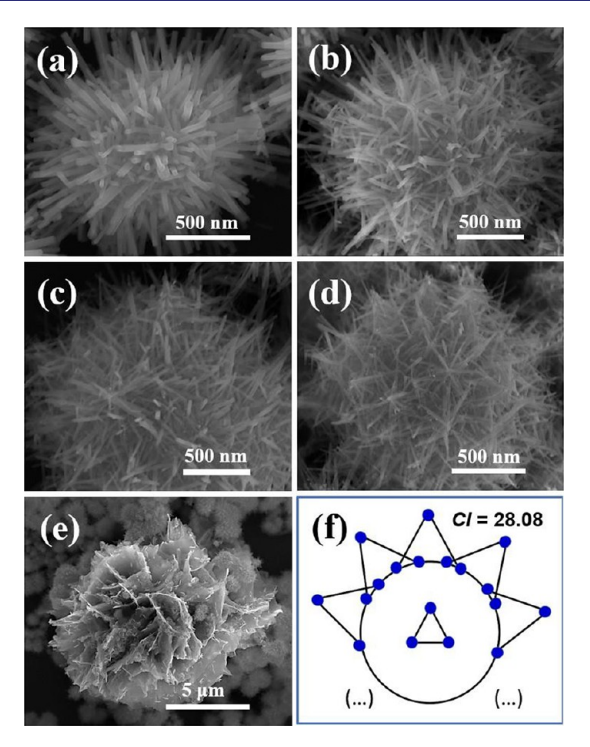


Figure 15. SEM images of CdS–Co₃O₄ phases assembled at different $W_{\rm R}$ at 160 °C for 20 h: (a) $W_{\rm R}$ = 0.0, (b) 0.06, (c) 0.12, (d) 0.60, and (e) 1.20. $W_{\rm R}$ is the weight ratio of Co₃O₄ to CdS. (f) GT representation of the FLP in (e). K_3 graph (i.e., triangle) inside a loop represents nanosheets assembled into a spherical SP of nonrandom size. A quasi-infinite sequence of K_3 graphs connected to a loop represents intersecting nanosheets in nonrandom radial orientation with respect to the surface of the SP. Only the geometrical complexity of the corrugated nanostructured microparticle was taken into account in these calculations. Incorporation of chemical complexity, i.e., the presence of two types of building blocks, Co₃O₄ and CdS NPs, will further increase CI.

reaction rates preferences, resulting in the self-assembly of nanosheets instead of NRs.

Understanding the fundamental mechanisms and assembly pathways of HPs and other complex self-assembled microparticles has obvious practical implications because it makes possible the formation of complex particles with unusually high dispersion stability, ¹⁵ biomimetic behavior, ⁵⁸ and novel (meta)optical properties. ⁵⁹ The efficient light absorption and dispersion behavior of CdS HPs enable their applications in photocatalysis, for instance in catalysis of butanol ³⁵ and liquid CO₂. Further studies in this direction will include a better understanding of the interplay of thermodynamic and kinetic parameters controlling the nanostructured features.

METHODS

Chemicals. Ethylenediamine (\geq 99.0%, Sigma-Aldrich), sodium diethyldithiocarbamate trihydrate (\geq 99.0%, Alfa Aesar), and cadmium chloride (\geq 99.99%, Sigma-Aldrich) were all used as received.

Synthesis of Cadmium Diethyldithiocarbamate. The metal complex was prepared through a simple precipitation reaction. Typically, 4.0 g of cadmium(II) chloride (CdCl₂) was dissolved in 50 mL of distilled water, followed by the addition of 16.0 g of sodium diethyldithiocarbamate. After being stirred and sonicated for 2 h, the product was washed three times with distilled water and ethanol.

Synthesis of CdS HPs. 0.0605 mmol of cadmium diethyldithiocarbamate was added into a 20 mL solvent mixture containing various amounts of distilled water and EA. The volume of distilled water was 8, 10, 12, and 15 mL. Then the resulting mixture was transferred into a Teflon-lined stainless autoclave. The autoclave was then sealed and maintained at 120, 140, 160, and 180 °C for 20 h to allow the growth of CdS HPs. Ice water was used to rapidly cool the hydrothermal reaction, followed by immediate analysis to acquire accurate temporal information about the early growth stages. After that, hedgehog-like products were collected via centrifugation and washed three times with deionized water.

All the hydrothermal reactions occurred in autoclaves with a volume of 30 mL. When the oven reached the set temperature for hydrothermal reaction, the autoclave was placed into the oven to allow the growth of CdS HPs. No shaking or stirring was applied during the hydrothermal reaction.

Synthesis of NP Dispersions at Room Temperature. 20 mL of EA and distilled water were added into a centrifuge tube with 0.0605 mmol of cadmium diethyldithiocarbamate and then sonicated to make the cadmium diethyldithiocarbamate dissolve completely. The obtained solution was then aged at ambient temperature for 20 h.

Synthesis of Mixed Assemblies of CdS and Co_3O_4 NPs. Typically, 0.0605 mmol of cadmium diethyldithiocarbamate was added into a 20 mL solvent mixture containing 10 mL of distilled water and 10 mL of EA, sonicated for 1 min, and aged at room temperature for 1 day. Then Co_3O_4 NPs according to the previously published protocol. Finally, all of the mixture was transferred to a Teflon-lined stainless autoclave, maintained at 160 °C for 20 h to allow the growth of CdS– Co_3O_4 assemblies. Weight ratios of Co_3O_4 to CdS, W_B , ranged from 0, 0.06, 0.12, and 0.60 to 1.20.

Characterization. Scanning electron microscopy (SEM) images and energy-dispersive X-ray (EDX) spectroscopy data were acquired by a FEI Helios Nanolab 650 dual-beam system. Transmission electron microscopy (TEM) and high-resolution scanning transmission electron microscopy (HR-STEM) images were obtained by using a JEOL-3100R05 double-corrected S/TEM operated at 300 kV. Element-mapping and tomography series were performed by using a Thermo Fisher Scientific Talos F200X G2 S/TEM equipped with a Super-X EDX detector. The tomography data set was acquired by tilting the sample from -70° to 70° with an increment of 2° . The 3D reconstruction was performed with the simultaneous iterations reconstruction technique (SIRT) algorithm using the reconstruction module in Gatan Digital Micrograph. Powder X-ray diffraction (XRD) experiments were performed on a Rigaku rotating anode X-ray diffractometer using Cu K α radiation (1.54 Å) to determine the crystal structure of the nanocrystals. Raman spectra were obtained on a Renishaw inVia microscope at room temperature (Ar ion laser, 532 nm). Optical absorption spectra were measured at room temperature by using an Agilent 8453 UV-vis spectrophotometer.

The center of the HPs is too dense to be imaged by TEM or other methods of electron microscopy.

Lengths of spikes were estimated by assuming that the inner dark part of TEM images of HPs is circular ("core") and represents SPCS. The lengths of spikes are estimated as the average distances between the tips of spikes and the circle. Performing statistical analysis of the spike lengths, 30 spikes were measures three times each. The number of spikes per $\mu \mathrm{m}^2$ was obtained from the analysis of SEM images. Typically, we set a 1 $\mu \mathrm{m} \times 1~\mu \mathrm{m}$ square and count the number of spikes within this size of the area. Every ten different areas were analyzed three times, and the resulting data were averaged.

ASSOCIATED CONTENT

Supporting Information

The Supporting Information is available free of charge at https://pubs.acs.org/doi/10.1021/jacs.1c05488.

Additional characterizations on the size, shape, crystal structure, and optical properties of the products and the samples obtained by optimizing synthetic conditions or during the assembly process of NPs, including Figures S1–S14 (PDF)

Video S1: TEM tomography of CdS hedgehog particle (PPTX)

AUTHOR INFORMATION

Corresponding Authors

Sharon C. Glotzer — Department of Chemical Engineering, University of Michigan, Ann Arbor, Michigan 48109, United States; Biointerfaces Institute, University of Michigan, Ann Arbor, Michigan 48109, United States; orcid.org/0000-0002-7197-0085; Email: sglotzer@umich.edu

Nicholas A. Kotov — Department of Chemical Engineering, University of Michigan, Ann Arbor, Michigan 48109, United States; Biointerfaces Institute, University of Michigan, Ann Arbor, Michigan 48109, United States; orcid.org/0000-0002-6864-5804; Email: kotov@umich.edu

Authors

Lanqin Tang — Department of Chemistry and Chemical Engineering, Yancheng Institute of Technology, Yancheng, Jiangsu 224051, P. R. China; Department of Chemical Engineering, University of Michigan, Ann Arbor, Michigan 48109, United States; Biointerfaces Institute, University of Michigan, Ann Arbor, Michigan 48109, United States

Thi Vo — Department of Chemical Engineering, University of Michigan, Ann Arbor, Michigan 48109, United States; Biointerfaces Institute, University of Michigan, Ann Arbor, Michigan 48109, United States

Xiaoxing Fan — Department of Chemical Engineering, University of Michigan, Ann Arbor, Michigan 48109, United States; School of Physics, Liaoning University, Shenyang, Liaoning 110036, P. R. China; orcid.org/0000-0001-5679-7395

Drew Vecchio — Department of Chemical Engineering, University of Michigan, Ann Arbor, Michigan 48109, United States

Tao Ma – Michigan Center for Materials Characterization, University of Michigan, Ann Arbor, Michigan 48109-2102, United States; Department of Materials Science, University of Michigan, Ann Arbor, Michigan 48109, United States

Jun Lu — Department of Chemical Engineering, University of Michigan, Ann Arbor, Michigan 48109, United States; Biointerfaces Institute, University of Michigan, Ann Arbor, Michigan 48109, United States; orcid.org/0000-0001-7029-855X

Harrison Hou – Department of Chemical Engineering, University of Michigan, Ann Arbor, Michigan 48109, United States; Biointerfaces Institute, University of Michigan, Ann Arbor, Michigan 48109, United States

Complete contact information is available at: https://pubs.acs.org/10.1021/jacs.1c05488

Author Contributions

L.T. and T.V. contributed equally to this work.

Notes

The authors declare no competing financial interest.

ACKNOWLEDGMENTS

The central part of this work was supported by the Department of the Navy, Office of Naval Research under ONR award number N00014-18-1-2497. Support was also provided by the National Science Foundation Award # CMMI 1463474 "Energy- and Cost-Efficient Manufacturing Employing Nano-

particles" and by a DoD Vannevar Bush Faculty Fellowship to N.A.K. titled "Engineered Chiral Ceramics" ONR Award No. N000141812876. Additionally, National Science Foundation Division Of Chemistry Award # 1566460 "Nanospiked Particles for Photocatalysis" and Division Of Civil, Mechanical, & Manufacturing Innovation Award # 1538180 "Layered Composites from Branched Nanofibers for Lithium Ion Batteries" are also gratefully acknowledged. Computational work utilized the Extreme Science and Engineering Discovery Environment (XSEDE), 60 which is supported by National Science Foundation grant number ACI-1548562; XSEDE award DMR 140129, and was also supported in part through computational resources and services supported by Advanced Research Computing at the University of Michigan, Ann Arbor. Michigan Center for Materials Characterization (MC)² is acknowledged for its assistance with electron microscopy and the NSF Grant #DMR-9871177 for funding of the JEOL 2010F analytical electron microscope used in this work. We greatly acknowledge financial assistance by China Scholarship Council to L.T. and X.F.

REFERENCES

- (1) Kawai, T.; Sakata, T. Hydrogen Evolution from Water Using Solid Carbon and Light Energy. *Nature* **1979**, 282 (5736), 283–284.
- (2) Zou, Z.; Ye, J.; Sayama, K.; Arakawa, H. Direct Splitting of Water under Visible Light Irradiation with an Oxide Semiconductor Photocatalyst. *Nature* **2001**, *414* (6864), 625–627.
- (3) Lin, B.; Yang, G.; Wang, L. Stacking-Layer-Number Dependence of Water Adsorption in 3D Ordered Close-Packed g-C3N4 Nanosphere Arrays for Photocatalytic Hydrogen Evolution. *Angew. Chem., Int. Ed.* **2019**, 58 (14), 4587–4591.
- (4) Takata, T.; Jiang, J.; Sakata, Y.; Nakabayashi, M.; Shibata, N.; Nandal, V.; Seki, K.; Hisatomi, T.; Domen, K. Photocatalytic Water Splitting with a Quantum Efficiency of Almost Unity. *Nature* **2020**, *581* (7809), 411–414.
- (5) Tu, W.; Zhou, Y.; Zou, Z. Photocatalytic Conversion of CO₂ into Renewable Hydrocarbon Fuels: State-of-the-Art Accomplishment, Challenges, and Prospects. *Adv. Mater.* **2014**, *26* (27), 4607–4626.
- (6) Méndez, M. A.; Voyame, P.; Girault, H. H. Interfacial Photoreduction of Supercritical CO₂ by an Aqueous Catalyst. *Angew. Chem., Int. Ed.* **2011**, 50 (32), 7391–7394.
- (7) Kamada, K.; Jung, J.; Wakabayashi, T.; Sekizawa, K.; Sato, S.; Morikawa, T.; Fukuzumi, S.; Saito, S. Photocatalytic CO₂ Reduction Using a Robust Multifunctional Iridium Complex toward the Selective Formation of Formic Acid. *J. Am. Chem. Soc.* **2020**, *142* (23), 10261–10266.
- (8) Montjoy, D. G.; Hou, H.; Bahng, J. H.; Kotov, N. A. Omnidispersible Microscale Colloids with Nanoscale Polymeric Spikes. *Chem. Mater.* **2020**, *32* (23), 9897–9905.
- (9) Zhang, S.; Geryak, R.; Geldmeier, J.; Kim, S.; Tsukruk, V. V. Synthesis, Assembly, and Applications of Hybrid Nanostructures for Biosensing. *Chem. Rev.* **2017**, *117* (20), 12942–13038.
- (10) Kong, R.-M.; Zhang, X.-B.; Chen, Z.; Tan, W. Aptamer-Assembled Nanomaterials for Biosensing and Biomedical Applications. *Small* **2011**, *7* (17), 2428–2436.
- (11) Liu, S.; Jones, L.; Gu, F. X. Nanomaterials for Ocular Drug Delivery. *Macromol. Biosci.* **2012**, *12* (5), 608–620.
- (12) Yoneyama, H.; Yamashita, Y.; Tamura, H. Heterogeneous Photocatalytic Reduction of Dichromate on N-Type Semiconductor Catalysts. *Nature* **1979**, 282 (5741), 817–818.
- (13) Bandara, J.; Kiwi, J.; Pulgarin, C.; Peringer, P.; Pajonk, G.-M.; Elaloui, A.; Albers, P. Novel Cyclic Process Mediated by Copper Oxides Active in the Degradation of Nitrophenols: Implications for the Natural Cycle. *Environ. Sci. Technol.* **1996**, 30 (4), 1261–1267.
- (14) Sadeghi, M.; Liu, W.; Zhang, T.-G.; Stavropoulos, P.; Levy, B. Role of Photoinduced Charge Carrier Separation Distance in

- Heterogeneous Photocatalysis: Oxidative Degradation of CH3OH Vapor in Contact with Pt/TiO₂ and Cofumed TiO₂-Fe₂O₃. *J. Phys. Chem.* **1996**, *100* (50), 19466–19474.
- (15) Bahng, J. H. J. H.; Yeom, B.; Wang, Y.; Tung, S. O.; Hoff, J. D. D.; Kotov, N. A. Anomalous Dispersions of 'Hedgehog' Particles. *Nature* **2015**, *517* (7536), 596–599.
- (16) Zhai, T.; Fang, X.; Bando, Y.; Liao, Q.; Xu, X.; Zeng, H.; Ma, Y.; Yao, J.; Golberg, D. Morphology-Dependent Stimulated Emission and Field Emission of Ordered CdS Nanostructure Arrays. *ACS Nano* **2009**, 3 (4), 949–959.
- (17) Datta, A.; Chavan, P. G.; Sheini, F. J.; More, M. A.; Joag, D. S.; Patra, A. Growth, Optical, and Field Emission Properties of Aligned CdS Nanowires. *Cryst. Growth Des.* **2009**, *9* (9), 4157–4162.
- (18) Nan, Y.-X.; Chen, F.; Yang, L.-G.; Chen, H.-Z. Electrochemical Synthesis and Charge Transport Properties of CdS Nanocrystalline Thin Films with a Conifer-like Structure. *J. Phys. Chem. C* **2010**, *114* (27), 11911–11917.
- (19) Wu, W.; Wen, X.; Wang, Z. L. Taxel-Addressable Matrix of Vertical-Nanowire Piezotronic Transistors for Active and Adaptive Tactile Imaging. *Science* **2013**, 340 (6135), 952–957.
- (20) Duan, J. L.; Lei, D. Y.; Chen, F.; Lau, S. P.; Milne, W. I.; Toimil-Molares, M. E.; Trautmann, C.; Liu, J. Vertically-Aligned Single-Crystal Nanocone Arrays: Controlled Fabrication and Enhanced Field Emission. ACS Appl. Mater. Interfaces 2016, 8 (1), 472–479.
- (21) Sarkar, A.; Katiyar, A. K.; Mukherjee, S.; Singh, S.; Singh, S. K.; Das, A. K.; Ray, S. K. Geometry Controlled White Light Emission and Extraction in CdS/Black-Si Conical Heterojunctions. *ACS Appl. Electron. Mater.* **2019**, *1* (1), 25–33.
- (22) Wang, Y.; Tang, Z.; Liang, X.; Liz-Marzán, L. M.; Kotov, N. A. SiO₂-Coated CdTe Nanowires: Bristled Nano Centipedes. *Nano Lett.* **2004**, *4* (2), 225.
- (23) Xia, Y.; Nguyen, T. D. T. D.; Yang, M.; Lee, B.; Santos, A.; Podsiadlo, P.; Tang, Z.; Glotzer, S. C.; Kotov, N. A. Self-Assembly of Self-Limiting Monodisperse Supraparticles from Polydisperse Nanoparticles. *Nat. Nanotechnol.* **2011**, *6* (9), 580–587.
- (24) Supraparticles are defined as spontaneously formed assemblies of multiple nanoparticles following a distinctive pattern of preferred size and shape.
- (25) Liang, H.; Angelini, T. E.; Braun, P. V.; Wong, G. C. L. Roles of Anionic and Cationic Template Components in Biomineralization of CdS Nanorods Using Self-Assembled DNA-Membrane Complexes. *J. Am. Chem. Soc.* **2004**, *126* (43), 14157–14165.
- (26) Muruganandham, M.; Kusumoto, Y.; Okamoto, C.; Muruganandham, A.; Abdulla-Al-Mamun, M.; Ahmmad, B. Mineralizer-Assisted Shape-Controlled Synthesis, Characterization, and Photocatalytic Evaluation of CdS Microcrystals. *J. Phys. Chem. C* **2009**, *113* (45), 19506–19517.
- (27) Xiong, S.; Zhang, X.; Qian, Y. CdS with Various Novel Hierarchical Nanostructures by Nanobelts/Nanowires Self-Assembly: Controllable Preparation and Their Optical Properties. *Cryst. Growth Des.* **2009**, *9* (12), 5259–5265.
- (28) Wang, X.; Liu, M.; Zhou, Z.; Guo, L. Toward Facet Engineering of CdS Nanocrystals and Their Shape-Dependent Photocatalytic Activities. *J. Phys. Chem. C* **2015**, *119* (35), 20555–20560
- (29) Lin, Y.-F.; Song, J.; Ding, Y.; Lu, S.-Y.; Wang, Z. L. Alternating the Output of a CdS Nanowire Nanogenerator by a White-Light-Stimulated Optoelectronic Effect. *Adv. Mater.* **2008**, 20 (16), 3127–3130.
- (30) Simmons, B. A.; Li, S.; John, V. T.; McPherson, G. L.; Bose, A.; Zhou, W.; He, J. Morphology of CdS Nanocrystals Synthesized in a Mixed Surfactant System. *Nano Lett.* **2002**, *2* (4), 263–268.
- (31) Jiang, W.; Qu, Z.-b.; Kumar, P.; Vecchio, D.; Wang, Y.; Ma, Y.; Bahng, J. H.; Bernardino, K.; Gomes, W. R.; Colombari, F. M.; Lozada-Blanco, A.; Veksler, M.; Marino, E.; Simon, A.; Murray, C.; Muniz, S. R.; de Moura, A. F.; Kotov, N. A. Emergence of Complexity in Hierarchically Organized Chiral Particles. *Science* **2020**, 368 (6491), 642–648.

- (32) Kotov, N. A.; Dékány, I.; Fendler, J. H. Layer-by-Layer Self-Assembly of Polyelectrolyte-Semiconductor Nanoparticle Composite Films. *J. Phys. Chem.* **1995**, *99* (35), 13065–13069.
- (33) Tang, Z.; Zhang, Z.; Wang, Y.; Glotzer, S. C.; Kotov, N. A. Self-Assembly of CdTe Nanocrystals into Free-Floating Sheets. *Science* **2006**, 314 (5797), 274–278.
- (34) Caruso, F.; Caruso, R.; Moehwald, H. Nanoengineering of Inorganic and Hybrid Hollow Spheres by Colloidal Templating. *Science* **1998**, 282 (5391), 1111–1114.
- (35) Decher, G. Fuzzy Nanoassemblies: Toward Layered Polymeric Multicomposites. *Science* **1997**, 277 (5330), 1232–1237.
- (36) Wintzheimer, S.; Granath, T.; Oppmann, M.; Kister, T.; Thai, T.; Kraus, T.; Vogel, N.; Mandel, K. Supraparticles: Functionality from Uniform Structural Motifs. *ACS Nano* **2018**, *12* (6), 5093–5120.
- (37) Hou, K.; Han, J.; Tang, Z. Formation of Supraparticles and Their Application in Catalysis. *ACS Mater. Lett.* **2020**, 2 (1), 95–106. (38) Fu, Q.; Sheng, Y.; Tang, H.; Zhu, Z.; Ruan, M.; Xu, W.; Zhu,
- Y.; Tang, Z. Growth Mechanism Deconvolution of Self-Limiting Supraparticles Based on Microfluidic System. ACS Nano 2015, 9 (1), 172–179.
- (39) Montjoy, D. G.; Hou, H.; Bahng, J. H.; Eskafi, A.; Jiang, R.; Kotov, N. A. Photocatalytic Hedgehog Particles for High Ionic Strength Environments. ACS Nano 2021, 15, 4226.
- (40) Tang, Z.; Kotov, N. A.; Giersig, M. Spontaneous Organization of Single CdTe Nanoparticles into Luminescent Nanowires. *Science* **2002**, 297 (5579), 237–240.
- (41) De Yoreo, J. J.; Gilbert, P. U. P. A. P. A.; Sommerdijk, N. A. J. M. J. M.; Penn, R. L.; Whitelam, S.; Joester, D.; Zhang, H.; Rimer, J. D.; Navrotsky, A.; Banfield, J. F.; Wallace, A. F.; Michel, F. M.; Meldrum, F. C.; Cölfen, H.; Dove, P. M. Crystallization by Particle Attachment in Synthetic, Biogenic, and Geologic Environments. *Science* 2015, 349 (6247), No. aaa6760.
- (42) Querejeta-Fernàndez, A.; Hernàndez-Garrido, J. C.; Yang, H.; Zhou, Y.; Varela, A.; Parras, M.; Calvino-Gàmez, J. J.; Gonzàlez-Calbet, J. M.; Green, P. F.; Kotov, N. A. Unknown Aspects of Self-Assembly of PbS Microscale Superstructures. *ACS Nano* **2012**, *6* (5), 3800–3812.
- (43) Yang, M.; Sun, K.; Kotov, N. A. Formation and Assembly-Disassembly Processes of ZnO Hexagonal Pyramids Driven by Dipolar and Excluded Volume Interactions. *J. Am. Chem. Soc.* **2010**, 132 (6), 1860–1872.
- (44) Deng, D.; Hao, C.; Sen, S.; Xu, C.; Král, P.; Kotov, N. A. Template-Free Hierarchical Self-Assembly of Iron Diselenide Nanoparticles into Mesoscale Hedgehogs. *J. Am. Chem. Soc.* **2017**, *139* (46), 16630–16639.
- (45) Li, Y.; Girard, M.; Shen, M.; Millan, J. A.; Olvera de la Cruz, M. Strong Attractions and Repulsions Mediated by Monovalent Salts. *Proc. Natl. Acad. Sci. U. S. A.* **2017**, *114* (45), 11838–11843.
- (46) Daoud, M.; Cotton, J. P. Star Shaped Polymers: A Model For The Conformation And Its Concentration Dependence. *J. Phys.* **1982**, 43 (3), 531–538.
- (47) Luo, Y.; Zhao, R.; Pendry, J. B. Van Der Waals Interactions at the Nanoscale: The Effects of Nonlocality. *Proc. Natl. Acad. Sci. U. S. A.* **2014**, *111* (52), 18422–18427.
- (48) Silvera Batista, C. A.; Larson, R. G.; Kotov, N. A. Nonadditivity of Nanoparticle Interactions. *Science* **2015**, *350* (6257), 1242477.
- (49) Giorgi, F.; Coglitore, D.; Curran, J. M.; Gilliland, D.; Macko, P.; Whelan, M.; Worth, A.; Patterson, E. A. The Influence of Inter-Particle Forces on Diffusion at the Nanoscale. *Sci. Rep.* **2019**, 9 (1), 12689.
- (50) Zhang, H.; Wang, D. Controlling the Growth of Charged-Nanoparticle Chains through Interparticle Electrostatic Repulsion. *Angew. Chem., Int. Ed.* **2008**, *47* (21), 3984–3987.
- (51) Zhang, Z.; Tang, Z.; Kotov, N. A.; Glotzer, S. C. Simulations and Analysis of Self-Assembly of CdTe Nanoparticles into Wires and Sheets. *Nano Lett.* **2007**, *7* (6), 1670–1675.

- (52) Tang, Z.; Zhang, Z.; Wang, Y.; Glotzer, S. C.; Kotov, N. A. Self-Assembly of CdTe Nanocrystals into Free-Floating Sheets. *Science* (Washington, DC, U. S.) **2006**, 314 (5797), 274.
- (53) Raphael, E.; Pincus, P.; Fredrickson, G. H. Conformation of Star Polymers in High-Molecular-Weight Solvents. *Macromolecules* **1993**, 26 (8), 1996–2006.
- (54) de Gennes, P. G. Conformations of Polymers Attached to an Interface. *Macromolecules* **1980**, *13* (5), 1069–1075.
- (55) Smit, B.; Frenkel, D. Understanding Molecular Simulation; Academic Press: 2002.
- (56) Körber, C.; Rau, G.; Cosman, M. D.; Cravalho, E. G. Interaction of Particles and a Moving Ice-Liquid Interface. *J. Cryst. Growth* **1985**, 72 (3), 649–662.
- (57) Yeom, J.; Santos, U. S. S.; Chekini, M.; Cha, M.; de Moura, A. F.; Kotov, N. A. A. Chiromagnetic Nanoparticles and Gels. *Science* **2018**, 359 (6373), 309–314.
- (58) Zhao, L.; Song, X.; Ouyang, X.; Zhou, J.; Li, J.; Deng, D. Bioinspired Virus-like Fe₃O₄/Au@C Nanovector for Programmable Drug Delivery via Hierarchical Targeting. *ACS Appl. Mater. Interfaces* **2021**, *13*, 49631.
- (59) Bahng, J. H.; Jahani, S.; Montjoy, D. G.; Yao, T.; Kotov, N.; Marandi, A. Mie Resonance Engineering in Meta-Shell Supraparticles for Nanoscale Nonlinear Optics. *ACS Nano* **2020**, *14* (12), 17203–17212.
- (60) Towns, J.; Cockerill, T.; Dahan, M.; Foster, I.; Gaither, K.; Grimshaw, A.; Hazlewood, V.; Lathrop, S.; Lifka, D.; Peterson, G. D.; Roskies, R.; Scott, J. R.; Wilkins-Diehr, N. XSEDE: Accelerating Scientific Discovery. *Comput. Sci. Eng.* **2014**, *16* (5), 62–74.